Nanoscale Advances

ROYAL SOCIETY OF CHEMISTRY

PAPER

View Article Online
View Journal | View Issue

Cite this: *Nanoscale Adv.*, 2025, **7**, 7638

Synergistic effect of Mo doping on the pseudocapacitive performance of Zn–V–O based TMOs for supercapacitor applications

Pankaj Kumar Sharma,[a] Anshuman Sahai,[a] Deepti Maikhuri,[a] Santosh J. Uke,[b] Somya Asthana[c] and Yogesh Kumar *[d]

Supercapacitors (SCs) are crucial for meeting the growing demand for energy. The development of next-generation SCs still depends on the evolution of high-performance electrode materials. Compared with single component metal oxides, ternary metal oxides (TMOs) offer multiple oxidation states and superior supercapacitive performance. The rational design and doping of complex metal oxides offer a powerful strategy to overcome the performance limitations of supercapacitors (SCs). This work presents pure and Mo-doped ZnV_2O_4 ternary metal oxides (Mo-TMOs) with tailored nanostructures synthesized by a hydrothermal method to optimize the electrochemical performance for SC applications. The synthesized materials were used for assembling a symmetric SC device. Comprehensive structural and morphological analyses confirm a uniform Mo distribution and the formation of highly interconnected nanostructures that promote rapid ion diffusion and electron transport. The prepared ZnV_2O_4 and $ZnV_{0.98}Mo_{0.02}O_2$ deliver excellent specific capacitances of 697.14 F g^{-1} and 752.08 F g^{-1} at 5 mV s^{-1}, respectively. The fabricated device possesses a high energy density of 34.85 Wh kg^{-1} at a power density of 313.71 W kg^{-1} for ZnV_2O_4 and 37.60 Wh kg^{-1} at a power density of 323.08 W kg^{-1} for the $ZnV_{0.98}Mo_{0.02}O_2$ sample. Both samples possess high BET surface areas of 77.25 and 100.42 m^2 g^{-1}. Moreover, the fabricated device exhibits excellent cyclic stability of 96.1% for the pure sample and 97.2% for the Mo-doped sample at 5 A g^{-1} after 10 000 cycles. Incorporation of Mo into the ternary oxide framework successfully tunes the electronic conductivity, increases the redox activity and enhances the structural stability, indicating promising SC performances for future prospects.

Received 18th July 2025
Accepted 3rd October 2025

DOI: 10.1039/d5na00690b

rsc.li/nanoscale-advances

1. Introduction

Non-renewable energy sources based on fossil fuels are running out due to the continuously increasing global energy demands.[1] Therefore, it is an urgent need to develop a clean, environmentally conscious and sustainable energy source. This energy source should be a good substitute to fossil fuels and must fulfill the continuous requirement of energy. There are many renewable energy sources like solar energy, wind energy and tidal energy. However, energy from these sources are not continuously available, and hence, energy storage devices are needed.[2] This escalating demand for efficient and sustainable energy storage solutions has propelled SCs to the forefront of research due to their remarkable supercapacitive property, electrochemical behaviour and extended cycle life.[3–5] In comparison with batteries, SCs are compact, lightweight, and cost-effective and have a higher power density of more than 10 kW kg^{-1}, a longer life, the ability to rapidly charge as well as discharge, a broad working temperature range, and excellent cycle retention qualities greater than 100 000 cycles.[6–8] These practical values of SC parameters and the availability of electrode materials make them a prominent, sustainable and environment friendly energy storage device.[9–14] The unique benefit of SCs is that they can bridge the energy and power density gap between batteries and conventional capacitors.[15] However, their relatively low energy density compared to batteries remains a significant limitation. To address this, extensive efforts have been directed toward developing advanced electrode materials that can enhance the energy storage capacity and better the supercapacitive activities of SCs.[16]

Generally, an SC device is made up of two electrodes, two current collectors, an electrolyte, and a separator that physically separates the two electrodes.[8,17] Because of the porous nature of the electrode material, it helps in the charge storage

[a]*Department of Sciences (Physics), School of Sciences, Manav Rachna University, Faridabad-121004, Haryana, India*

[b]*Department of Physics, JDPS College, SGB Amravati University, Amravati 444803, India*

[c]*Department of Biotechnology, School of Engineering and Technology, Manav Rachna International Institute of Research and Studies, Faridabad, Haryana, India*

[d]*Department of Physics, Government PG College Sec-12, Palwal-121102, Haryana, India. E-mail: yk.physics@gmail.com; Tel: +91 9255533031*

mechanism.[18] SCs can be broadly classified into three categories, which are the electric double layer capacitor (EDLCs), pseudo capacitor (PCs) and the hybrid capacitor (HCs), which is prepared by the combination of the first two types.[17,19,20] However, there are only two categories of SCs on the basis of the charge storing mechanism. The first one is the electrical double layer capacitors (EDLCs) SCs and the other one is the pseudo supercapacitors (PCs).[21] Electrostatic charge storage at the conducting interface between the electrode and electrolyte is the basis for the electric double-layer capacitance (EDLCs) charge storage mechanism. This causes the Helmholtz double layer to develop. The formation of an electric double layer at the electrode–electrolyte interface allows ions to accumulate and store charge in EDLCs. The electrical energy is stored electrostatically *via* non-faradaic reaction at the electrode interface.[22,23] On the other hand, pseudocapacitance is a principle of electrical energy storage that relies on faradaic charge storage, in which electrons produced by reversible redox reactions are transferred across the electrode–electrolyte interface to electrochemically store the charge. Due to the highly reversible intercalation of electrolyte ions in the electrode material's lattice, no new chemical species are formed.[24] Furthermore, because more ions are utilized in the faradaic processes, pseudocapacitors deliver higher energy density and specific capacitance than the electric double layer capacitor.[25,26] The electrode material and synthesis methods are the key elements in the fabrication of high energy storage devices like SCs because they determine the performance of the SCs.[27,28] Therefore, the selection of the electrode materials and the synthesis methods are both crucial for enhancing the electrochemical performance of any SC device.[29]

Transition metal oxides have garnered considerable attention as electrode materials owing to their multiple oxidation states, which facilitate rich redox reactions, thereby contributing to high pseudocapacitance.[30,31] Despite these advantages, many transition metal oxides suffer from poor electrical conductivity and structural instability during cycling, which restrict their practical applications.[32] To overcome these challenges, researchers have explored the design of ternary metal oxides (TMOs), which incorporate three different metals into a single oxide framework using different synthesis methods. This strategy leverages the synergistic effects of various oxidation states among the constituent metals, leading to enhanced electrical conductivity, increased active sites, improved structural stability and better electrochemical performance.[33–35] Additionally, for improving the electrochemical activities of the SCs electrode materials, multiple ternary metal oxides were recently developed using various synthesis processes.[20,23] The hydrothermal technique is most commonly used for this purpose because it is simple, cost-effective, environmentally friendly and creates nanomaterials of the desired morphology and size.[36,37] In recent years, there have been many articles published on ternary metal oxides. Nimra *et al.* prepared TMOs through the hydrothermal method, which exhibited an excellent energy density of 138.9 Wh kg^{-1}. TMOs were created by Ferreira *et al.* using the Pechini process, which showed a specific capacitance of 328 F g^{-1} and an energy density of 18.92 Wh kg^{-1} at a power density of 345.7 W kg^{-1}.[38] Bhujun *et al.* synthesized nanocomposites by sol–gel method, which showed an excellent energy density of 7.9 kW kg^{-1} at 1 A g^{-1} and a specific capacitance of 221 F g^{-1} for CuCoF at a scan rate of 5 mV s^{-1}.[39] Co : Ni : MoO_4 were created by Xing *et al.* using the hydrothermal method, which showed an energy density of 12.5 Wh kg^{-1} and a high-power density of 7479.1 W kg^{-1}. Additionally, it demonstrated good cyclic stability and 91% capacity retention after 5000 cycles.[40] Huang *et al.* used a 1 : 2 : 2 ratio of Ni, Co, and Mo to create TMOs by the hydrothermal technique for SC applications. These electrode materials have a good energy density and a power density of 22.02 Wh kg^{-1} at 3.50 W kg^{-1}, and a capacitance value of 126 mF cm^{-2} at 10 mA cm^{-2}.[37] Furthermore, integrating TMOs with conductive materials, such as graphene or conducting polymers, or the doping of an additional metal has been shown to further boost their electrochemical properties. Qu *et al.* synthesized Mo-based ternary oxides (MTOs) *via* a facile and scalable method, which showed good value of energy and power density, but comparatively smaller specific capacitance value.[41] Sharma *et al.* fabricated a symmetric SC device based on a two-electrode system through a hydrothermal process. The fabricated device possessed an excellent specific capacitance of 573.21 F g^{-1} for the Mo-doped $MnV_{0.98}Mo_{0.02}O_2$. Furthermore, it exhibited high energy and power densities of 28.66 Wh kg^{-1} and 318.45 W kg^{-1}, respectively. This fabricated Mo-TMO also demonstrates superior cyclic stability of 96.1% after 5000 cycles.[17] Denis *et al.* synthesized an Mo-based ternary $Ni_{0.5}Co_{0.5}MoO_4 \cdot xH_2O$ by a scalable two-step method. The prepared ternary metal oxides exhibited better electrochemical performance by showing good energy and power density values as well as a better specific capacitance of 665.0 F g^{-1} at 5.0 A g^{-1}.[42] Teli *et al.* synthesized ternary metal oxides based on MnVMo-O by hydrothermal process, which demonstrated excellent electrochemical behavior.[43] Sharma *et al.* fabricated a symmetric TMO-based SC device using the hydrothermal method for SC applications. The as-fabricated device demonstrated superior supercapacitive properties for future prospects. This device shows the highest capacitance of 578.57 F g^{-1}, better energy density of 28.92 Wh kg^{-1} and power density of 318.34 W kg^{-1}. These TMOs also possess excellent material retention of 97.1% after 10 000 cycles.[44] These reports show that the TMO-based SCs synthesized by different synthesis methods can be a good approach for fulfilling the rising energy demand. A comparative analysis for the preparation of electrode materials by different synthesis methods is listed in Table 1. Based on the literature, it is clear that the hydrothermal method is not only a cost-effective method, but also provides better electrochemical performance.

This study explores the synthesis of pure and Mo-doped spinel ZnV_2O_4 TMOs for SC applications. ZnV_2O_4 is known for its rich redox activity and structural stability. However, its electrochemical performance is hindered by poor conductivity and limited active sites. Introducing Mo as a dopant into the ZnV_2O_4 lattice presents a novel strategy to overcome these challenges. Molybdenum, with its multiple valence states (Mo^{4+}/Mo^{6+}), plays a dual role: (i) it contributes additional redox centers, enhancing the pseudocapacitive behavior, and (ii) it

Table 1 Comparison of the synthesis methods for the preparation of different electrode materials

Material	Synthesis method	Specific capacitance	Energy density (E_d)	Power density (P_d)	Reference
TiO_2/NiO/ZnO	Electrospinning method	438 F g^{-1}	43.9 Wh kg^{-1}	749 W kg^{-1}	45
(NiO/ZnO@(GO)x)	Sol–gel method	1833.9 F g^{-1}	—	—	46
Mn-Ni-Co	Electrodeposition method	176.8 F g^{-1}	55.2 Wh kg^{-1}	749.91 W kg^{-1}	47
NiCoP	Solvothermal method	1095 F g^{-1}	43.54 Wh kg^{-1}	150 W kg^{-1}	48
PAni@Mg–OP/CuO	Co-precipitation method	702.8 F g^{-1}	37.5 Wh kg^{-1}	328.2 W kg^{-1}	34
Ag@MnCo-NGO-PVP	Hydrothermal method	1986.8 F g^{-1}	139.9 Wh kg^{-1}	5273.9 W kg^{-1}	49
CNT/P-(NiMn)Co_2O_4@NGQD	Hydrothermal method	2172 F g^{-1}	94.4 Wh kg^{-1}	800 W kg^{-1}	50
(NiO/V_2O_5/MnO_2)	Hydrothermal method	788 F g^{-1}	138 Wh kg^{-1}	450 W kg^{-1}	51

improves the electrical conductivity by modifying the electron transport pathways within the lattice.[52,53] Furthermore, Mo substitution promotes oxygen vacancies, which facilitate ion diffusion and boost charge storage capacity. This study shows the superior electrochemical performance of the Mo-doped ZnV_2O_4 sample, which introduces synergistic effects that enhance the redox activity and boost the electrical conductivity of the material. These synergistic effects are scarcely reported for the Zn–V–O system, especially in optimized doping concentrations and synthesized *via* a hydrothermal approach. Thus, this work not only introduces a novel doped ternary system, but also sets a precedent for tailoring spinel oxides *via* hetero-valent ion engineering to meet the performance demands of next-generation supercapacitors.

2. Experimental

2.1 Materials

We bought zinc acetate dihydrate ($Zn(CH_3COO)_2\cdot 2H_2O$), ammonium metavanadate (NH_4VO_3), ammonium molybdate ($(NH_4)_6Mo_7O_{24}\cdot 4H_2O$) and polyethylene glycol 400 (PEG-400) ($H(OCH_2CH_2)_nOH$) from Sigma-Aldrich. Urea (NH_2CONH_2) and hydrogen peroxide (H_2O_2) were imported from Thermo Fisher Scientific India Pvt., Ltd. We purchased graphite sheets (250 μm thick) from Nikunj Eximp Enterprises, Ltd, Bangalore. The solvents used for the entire synthesis process were ethanol and deionized water (DIW), which were purchased from Thermo Fisher Scientific.

2.2 Synthesis of ZnV_2O_4 electrode materials

A simple hydrothermal synthesis method following calcination treatment was used to synthesize the zinc, vanadium, and molybdenum-based nanostructured materials. The synthesis of the nanostructured ZnV_2O_4 was carried out by taking 5.47 g zinc acetate dihydrate ($Zn(CH_3COO)_2\cdot 2H_2O$) in 50 mL deionized water and 5.85 g of ammonium metavanadate (NH_4VO_3) in 50 mL deionized water (DIW). Both materials were magnetically stirred separately for 10 min at 40 °C. Subsequently, 5 mL polyethylene glycol 400 (PEG-400) ($H(OCH_2CH_2)_nOH$) and 2 g of urea (NH_2CONH_2) were added to the second material and magnetically stirred, and then, zinc acetate dihydrate ($Zn(CH_3COO)_2\cdot 2H_2O$) was added dropwise. This mixture was magnetically stirred again for one hour at 60 °C. After that, the prepared mixture was put inside a stainless-steel autoclave hydrothermal reactor lined with Teflon. For 12 hours, this mixture was heated up to 150 °C in a hot air oven. The autoclave was allowed to cool to room temperature once the reaction was finished. The produced sample was gathered, repeatedly cleaned with ethanol and deionized water using a centrifugation process (5000 rpm for 5–6 min), and then dried in a muffle furnace for 6 hours at 150 °C. Finally, the material was calcinated at 750 °C for 12 hours. The as-prepared pure ZnV_2O_4 was taken as sample S1. Similarly, another sample S2 ($ZnV_{0.98}Mo_{0.02}O_2$) was prepared by taking 5.47 g zinc acetate dihydrate and 5.73 g of ammonium metavanadate in 50 mL deionized water. Also, 0.62 g of ammonium molybdate ($(NH_4)_6Mo_7O_{24}\cdot 4H_2O$) was taken in another 50 mL deionized water. In this sample, magnetically stirred ammonium molybdate ($(NH_4)_6Mo_7O_{24}\cdot 4H_2O$) was added dropwise in place of zinc acetate dihydrate ($Zn(CH_3COO)_2\cdot 2H_2O$), and the rest of the procedure was the same as in the case of S1. A small portion of the synthesized ternary metal oxides was retained for several structural, vibrational, and morphological characterizations, whereas the main portion of materials would be used for electrode manufacturing, electrochemical characterization and device fabrication.

2.3 Fabrication of the supercapacitor device

For the fabrication of the SC device, a two-electrode system was used. The supercapacitor device was fabricated using similar types of materials for both electrodes on a graphite substrate of 1 cm^2. Throughout the entire fabrication process, polyvinylidene fluoride (PVDF) served as the binder and acetylene black served as the conducting agent. A fixed 80 : 10 : 10 ratio was maintained for the synthesized material, conductive additive (acetylene black) and binder (PVDF), respectively. All of the materials were ground with a mortar and pestle in order to form a homogeneous mixture, and then 0.5 mL of *N*,*N*-dimethylformamide (DMF) ($HCON(CH_3)_2$) solvent was added to form a slurry. This homogeneous slurry was coated on to a graphite substrate (1 cm^2) by paint brush and then dried in a hot air oven overnight at 60 °C. A highly sensitive electrical balance was used to determine the weight of the active mass that was put onto the graphite electrode. The deposited mass of the synthesized material on the graphite substrate was determined by measuring the mass of the graphite sheet before and after covering the mass of the dynamic material. In each case, the mass of the electrode material was found to be 0.0028 g. For

device characterization, 1 M of Na_2SO_4 was used as an electrolyte. As Na_2SO_4 is a neutral electrolyte, it is less corrosive, possesses a wide potential window and does not react with the electrode materials, which can otherwise cause device degradation.[54] A Whatman filter paper was used as a separator. The symmetric SC device was fabricated by sandwiching the Whatman filter paper between two similar types of electrodes after dipping it into 1 M of Na_2SO_4 electrolyte. The device was then placed in a sample holder for the electrochemical characterizations.

3. Characterization

3.1 Structural and morphological characterizations

In order to examine the phase and structural information of the prepared nanostructured materials, X-ray diffraction (Rigaku Miniflex X-ray diffractometer) with Cu Kα radiation at 1.5418 Å was utilized. The synthesized materials were examined by field emission scanning electron microscope (FESEM) by Gemini-SEM 560 for studying the surface morphological information and particle size. To study the different vibrational peaks that correspond to different stretching and bending modes, Fourier transform infrared spectroscopy (Shimadzu IR Spirit-T FTIR) was utilized. The surface area of the synthesized electrode materials was determined using a Brunauer–Emmett–Teller (BET) surface area analyzer (Quantachrome Instruments v10.0, Japan).

3.2 Electrochemical characterizations

An electrochemical workstation (CHI-680) setup was used for the electrochemical characterizations of the synthesized electrode materials. For the electrochemical characterization, a two-electrode system was used. 1 M of Na_2SO_4 was utilized as an electrolyte within the potential window of 0 V to 0.6 V for the CV and GCD analysis of the prepared electrode materials. In order to conduct an electrochemical impedance spectroscopy (EIS) study, an open circuit AC source with a frequency range of 1 mHz to 1 MHz was used.

The following four equations were used to determine the performance parameters of the synthesized electrode materials. Eqn (1) was used to determine the value of the specific capacitance C_s (F g^{-1}). Eqn (2) and (3) were used to determine the energy density E_d (Wh kg^{-1}) and power density P_d (W kg^{-1}) of the fabricated device, respectively. The coulombic efficiency was calculated by eqn (4).[55–57]

$$C_s(\mathrm{F\ g^{-1}}) = \frac{\int_{V_1}^{V_2} I(V)\mathrm{d}V}{mv(V_2 - V_1)} \quad (1)$$

$$E_d(\mathrm{Wh\ kg^{-1}}) = \frac{1}{2}\frac{C_s \Delta V^2}{3.6} \quad (2)$$

$$P_d(\mathrm{W\ kg^{-1}}) = \frac{E_d}{t_d} \times 3600 \quad (3)$$

$$\eta = \frac{t_d}{t_c} \times 100\% \quad (4)$$

Here, $\Delta V^2 = {V_{max}}^2 - {V_{min}}^2$, C_s represents the specific capacitance, I (mA) is the response current produced in the device, m (g) is the mass of the electrode material deposited onto the graphite substrate and ΔV represents the potential window. The terms t_c and t_d represent the charging and discharging times, respectively.

4. Results and discussion

4.1 X-ray diffraction (XRD) analysis

A Rigaku Miniflex X-ray diffractometer with Cu Kα radiation at 1.5418 Å was used to examine the phase, purity and crystallographic structural information of the synthesized materials. The XRD patterns of the samples S1 and S2 in the 2θ range of 10° to 80° are shown in Fig. 1, demonstrating how well the resulting XRD pattern is obtained. The characteristic peaks of sample S1 at 18.2°, 30°, 35.4°,43.1°, 53.3°, 56.7°, 62.5° and 66.2° and of sample S2 at 18.4°, 30.1°, 35.3°, 43.1°, 53.3°, 56.1°, 62.5° and 67.2° correspond to planes (111), (220), (311), (400), (422), (511), (440) and (533), respectively. The obtained diffraction patterns of the prepared samples were compared to the standard JCPDS card number 75-0318 to confirm the formation of the spinel structure, phase purity and peaks.[58–61] The Scherrer eqn (5) was used to calculate the crystallite size (D) of the materials.[62,63]

$$D = \frac{K\lambda}{\beta \cos\theta} \quad (5)$$

Here, K is the Scherrer constant (0.9), λ is the wavelength of the X-ray (Kα = 1.5418 Å), β is the full width at half maximum (FWHM) of the peak, and θ is Bragg's diffraction angle. The average crystallite size for each was found to be 47.8 nm and 32.6 nm. This suggest that after the doping of Mo in S2, the average crystallite size decreases, which increases the surface area. This increased surface area will be beneficial for ion diffusion and charge storage. The experimental data and sharpness of the XRD peaks show the high crystallinity spinel structure of the synthesized materials. The peaks of the Mo-

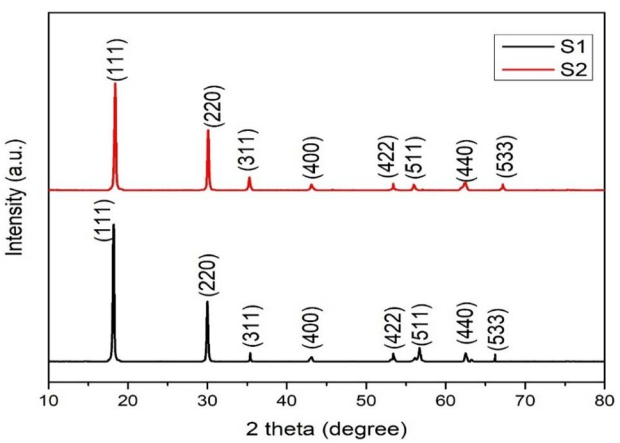

Fig. 1 XRD patterns of samples S1 and S2.

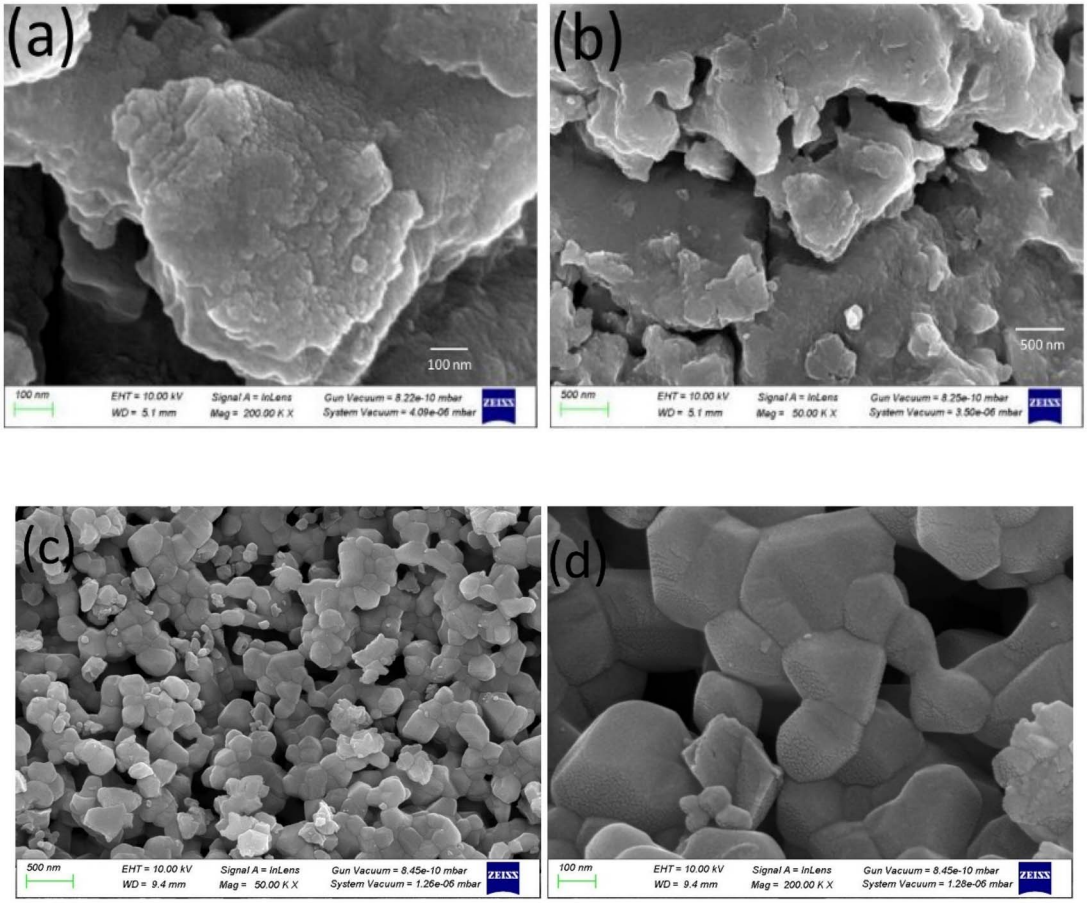

Fig. 2 FESEM images of sample S1 at (a) 100 nm and (b) 500 nm and S2 at (c) 100 nm and (d) 500 nm.

doped sample show a slight shift and broadening of peaks as compared to the undoped sample, indicating lattice distortion due to Mo-incorporation.[64] No significant impurity peaks are observed, which confirms the retention of the spinel structure of ZnV_2O_4 even after Mo-doping.

4.2 Field emission scanning electron microscope (FESEM) analysis

A Gemini-SEM 560 system with magnifications from 10× to 1 000 000× and good spatial resolution (~0.5 nm) was used to study the surface morphology and particle size of the

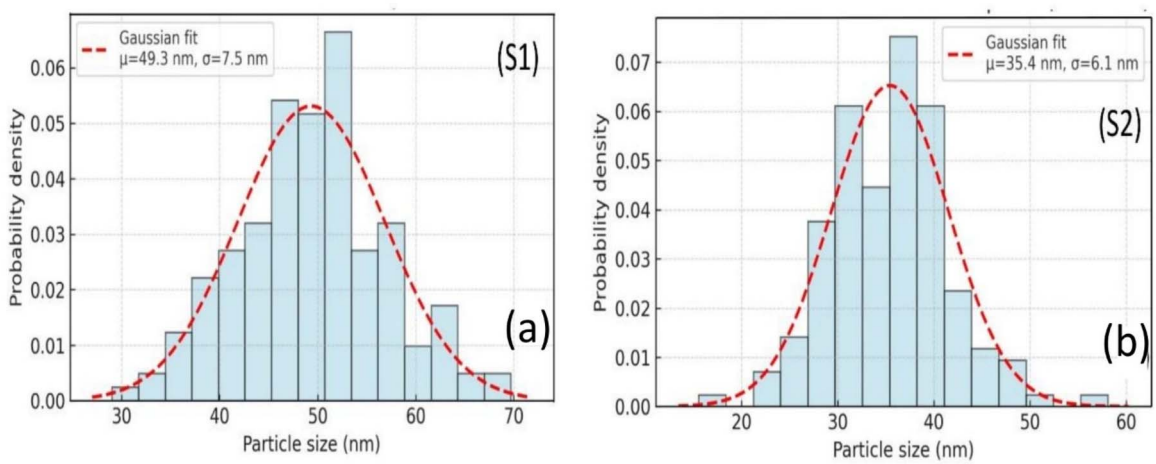

Fig. 3 Particle size histograms of samples S1 (a) and S2 (b).

synthesized samples. Fig. 2 displays the FESEM images of samples S1 and S2. The spinel-like structures and homogeneous morphology of the sample surfaces can be clearly seen from these micrographs. The microcracks and grain boundaries show the high degree of crystallinity of the synthesized samples. Particle sizes were measured quantitatively using ImageJ

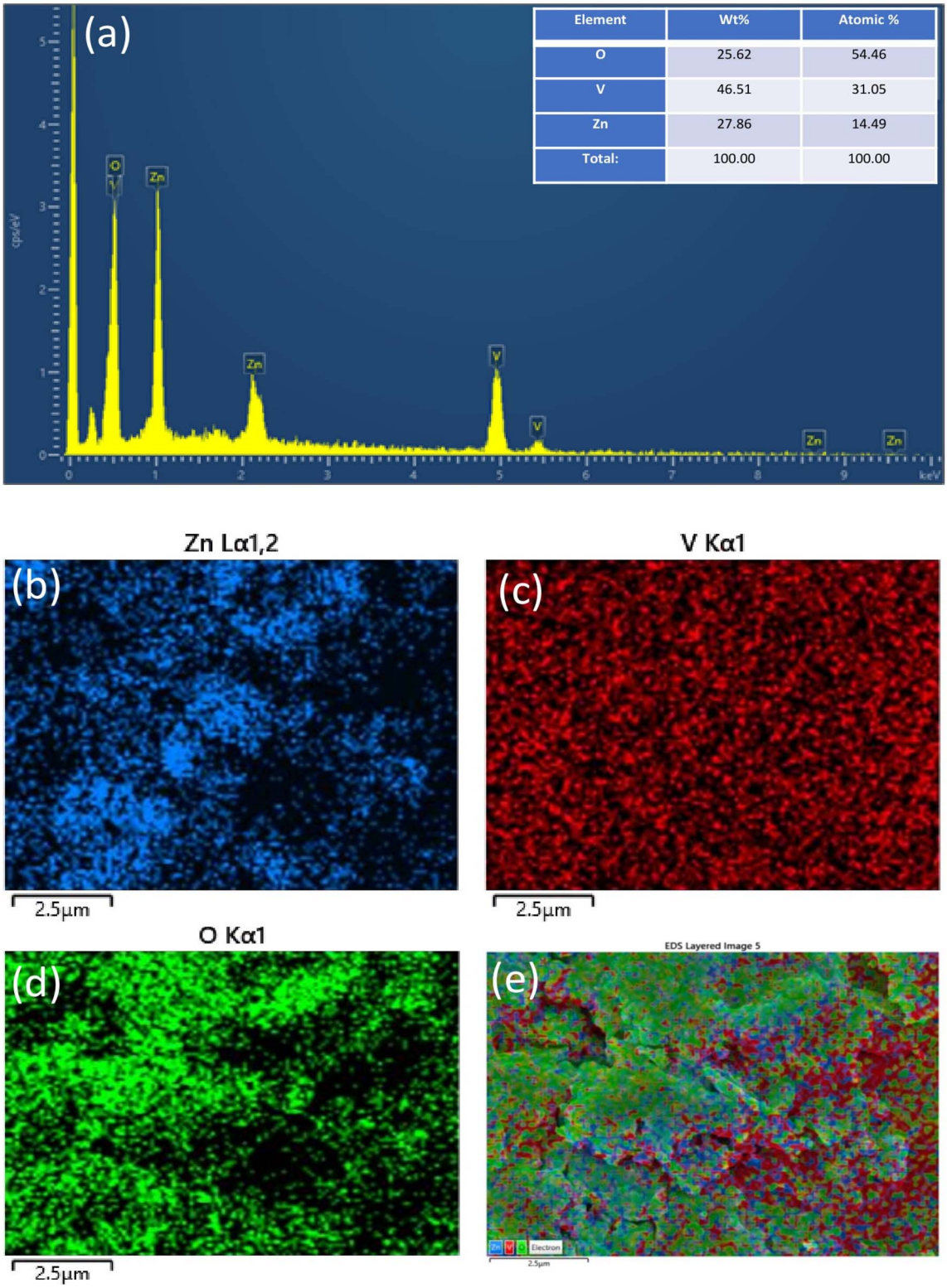

Fig. 4 (a) EDX spectra of S1, (b–d) elemental mapping of Zn, V and O and (e) elemental mapping of ZnV_2O_4.

software and Gaussian fitting was applied to the prepared histogram, as shown in Fig. 3. This shows the average particle size of 49.3 nm and 35.4 nm for S1 and S2, respectively, which is advantageous for improved electrochemical performance. Mo doping in ZnV_2O_4 results in an enhanced surface roughness, which increases the surface activity for catalytic applications

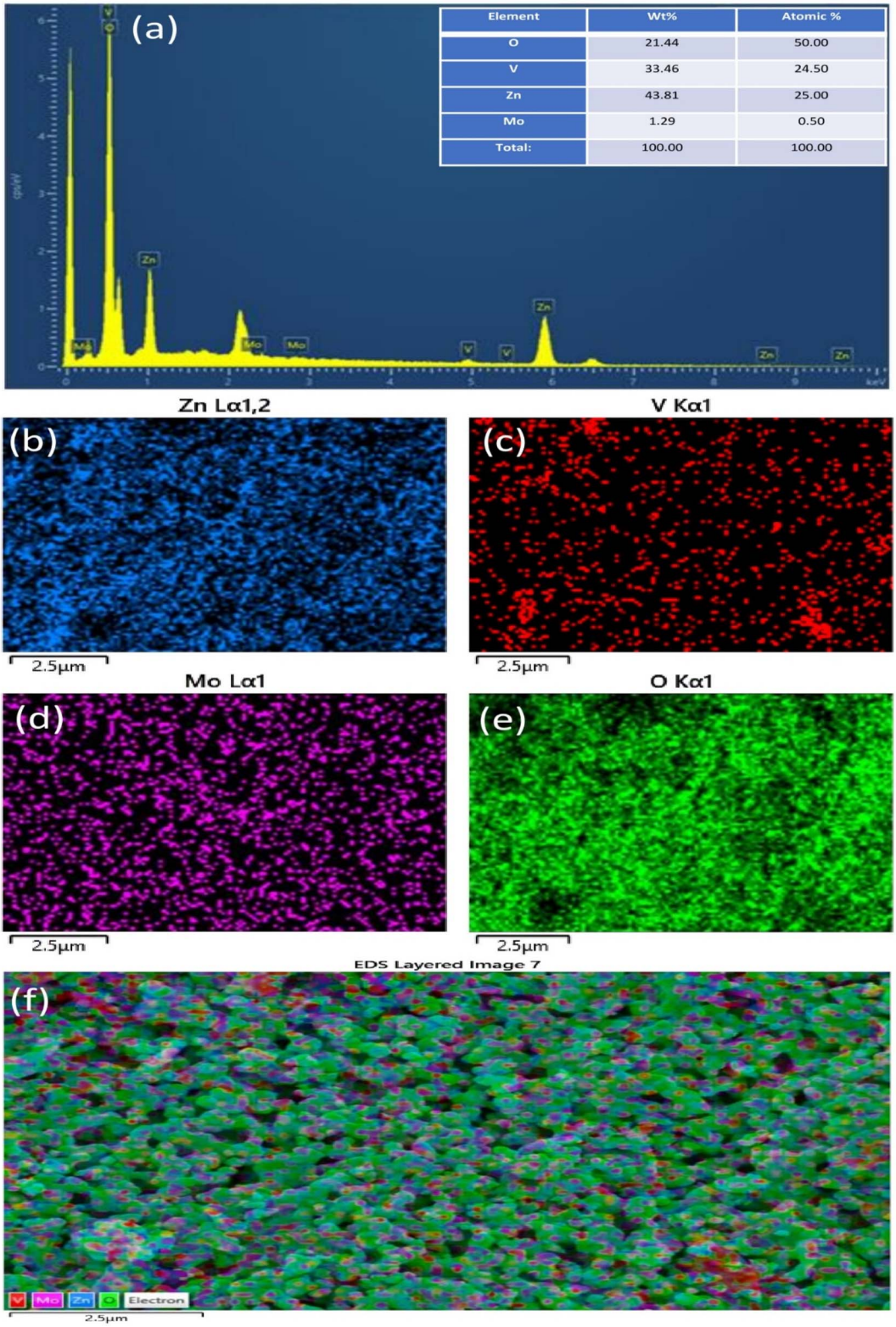

Fig. 5 (a) EDX spectra of S2, (b–e) elemental mapping of Zn, V, Mo and O and (f) elemental mapping of $ZnV_{0.98}Mo_{0.02}O_2$.

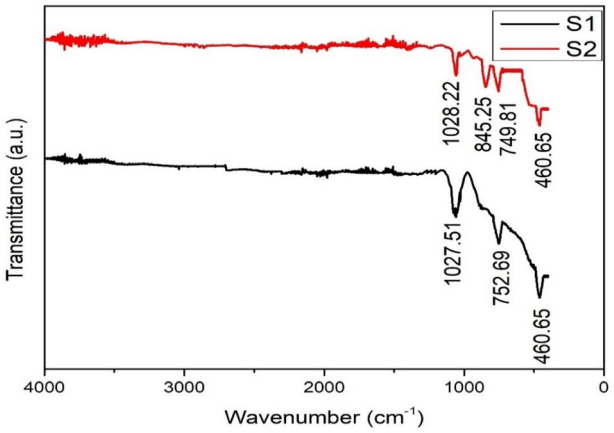

Fig. 6 FTIR spectra of samples S1 and S2.

without substantially altering the basic spinel structure. The samples were also examined using EDX spectra, which are displayed in Fig. 4 and 5 for samples S1 and S2, respectively. These spectra reveal that the elements in samples S1 and S2 are distributed uniformly.

4.3 Fourier transform infrared spectroscopy (FTIR) analysis

FTIR analysis using a Shimadzu IR Spirit-T system was done to assess the structural integrity and electrochemical relevance of ZnV_2O_4 for SCs application, and its spectra were analyzed. The FTIR spectra of samples S1 and S2 are displayed in Fig. 6. The distinctive absorption bands in this spectrum are attributed to M–O vibrations and other potential stretching and vibration modes. In this spectrum, a prominent band at 1028 cm^{-1} is attributed to V=O stretching, signifying the presence of electrochemically active vanadyl bonds. Bands at 750 and 469.65 cm^{-1} confirm the formation of a stable V–O–V and Zn–O lattice framework and spinel ZnV_2O_4 structure. FTIR analysis of the samples shows the presence of Zn–O and V–O vibrational peaks and the main spinel band remains at nearly the same position after Mo incorporation, which confirms that the original spinel structure remains intact even after Mo-incorporation. The Mo-doped sample shows an additional Mo–O stretching band at 845.25 cm^{-1}, which confirms successful Mo-doping without changing its original spinel structure. The metal–oxygen vibrations play a vital role in ensuring structural robustness and enabling faradaic redox activity crucial for pseudocapacitive performance. This structural motif facilitates efficient charge transport and enhances ion diffusion pathways, both of which are essential for high-rate charge–discharge cycling.

4.4 Brunauer–Emmett–Teller (BET) analysis

The capacitance of SCs depends on the surface area. Therefore, in order to determine the surface area of the as-synthesized pure and Mo-doped ZnV_2O_4 electrode materials, a Brunauer–Emmett–teller (BET) surface area analyzer (Quantachrome Instruments v10.0, Japan) was used. Fig. 7 shows the nitrogen adsorption and desorption isotherms for samples S1 and S2. The gradual increase in adsorption volume within the relative pressure range of 0.1 to 0.9 confirms the mesoporous structure of the materials, while the higher adsorption in S2 suggests an enhanced surface area and pore volume compared to S1. For both samples, the surface area was found to be 77.25 and 100.42 m^2 g^{-1}. This suggests that Mo doping in sample S2 with a higher surface area may have led to a more porous structure, which creates an abundance of active sites for ion adsorption and desorption and better electrochemical performance compared to pure sample S1.[65]

4.5 Electrochemical analysis

4.5.1 Cyclic voltammetry (CV) analysis. Cyclic voltammetry (CV) analysis was done using an electrochemical workstation (CHI-680) to study the supercapacitive performance of the prepared device made from pure (S1) and Mo-doped (S2)

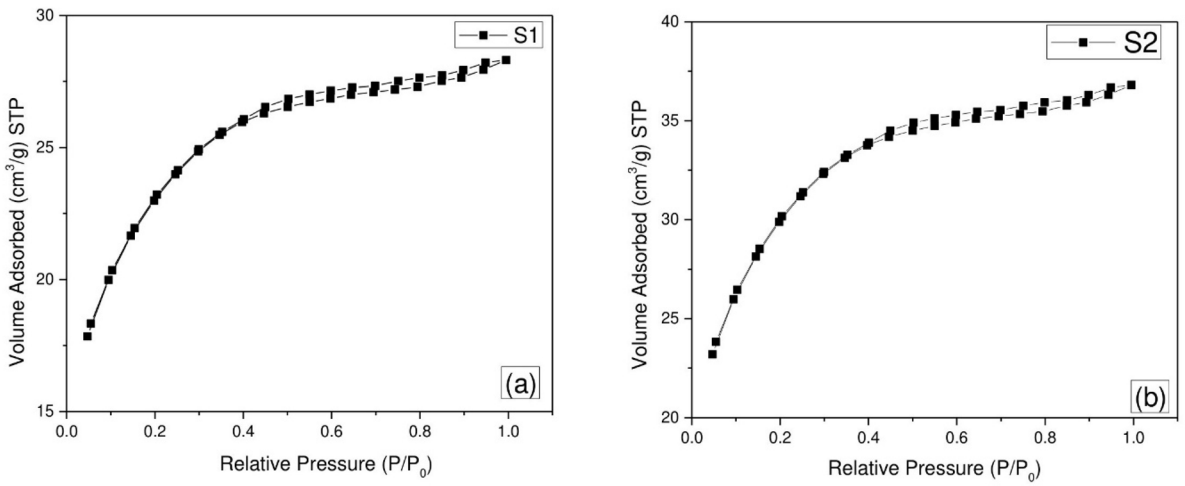

Fig. 7 Adsorption–desorption isotherms for (a) S1 and (b) S2.

electrode materials. Fig. 8 displays the CV curves of the pure and Mo-doped ZnV_2O_4 electrode materials in the potential range of 0 to 0.6 V and scan rate varying between 5 to 100 mV s^{-1}. The pseudocapacitive character of the pure and Mo-doped ZnV_2O_4 samples is clearly visible by the obtained CV curves. The shapes of the synthesized samples S1 and S2 are almost similar, but sample S2 exhibits a larger area under the CV curve than sample S1. The maximum specific capacitance value for samples S1 and S2 was found to be 697.14 F g^{-1} and 752.08 F g^{-1}, respectively, at a scan rate of 5 mV s^{-1}. The charge storage mechanism of the pure and Mo-doped nanocrystalline ZnV_2O_4 electrode materials is primarily driven by the surface phenomenon of alkali cation intercalation and de-intercalation.[66,67] Pure and Mo-doped electrodes at different scan rates are compared, along with their corresponding capacitance values, in Table 2. The CV analysis results show that the specific capacitance values decreased at higher scan rates for the synthesized samples. The specific capacitance may decrease due to the presence of interior active sites that cannot completely support the redox transition at higher scan rates.[68,69] The power law formula given by eqn (6) was used to calculate the charge storage mechanism and quantify the contributions from diffusion and capacitance to the prepared materials. CV analysis shows both types of charge storage mechanisms (capacitive and diffusion) for S1 and S2. Therefore, they can perform better as SC devices. The fitting parameters k_1 and k_2 were determined to be 1 and 1.49 for S1, and 1 and 0.75 for sample S2, respectively. These values correspond to a capacitive contribution of around 60% at a scan rate of 5 mV s^{-1} for S1. Meanwhile, the Mo-doped sample S2 shows an enhanced capacitive contribution of about 75% at the same

Table 2 Comparison of the specific capacitance of samples S1 and S2 at different scan rates

S. no.	Scan rate (mV s^{-1})	Specific capacitance (F g^{-1}), S1	Specific capacitance (F g^{-1}), S2
1.	5	697.14	752.08
2.	10	598.63	607.26
3.	50	273.69	298.73
4.	100	186.55	194.17

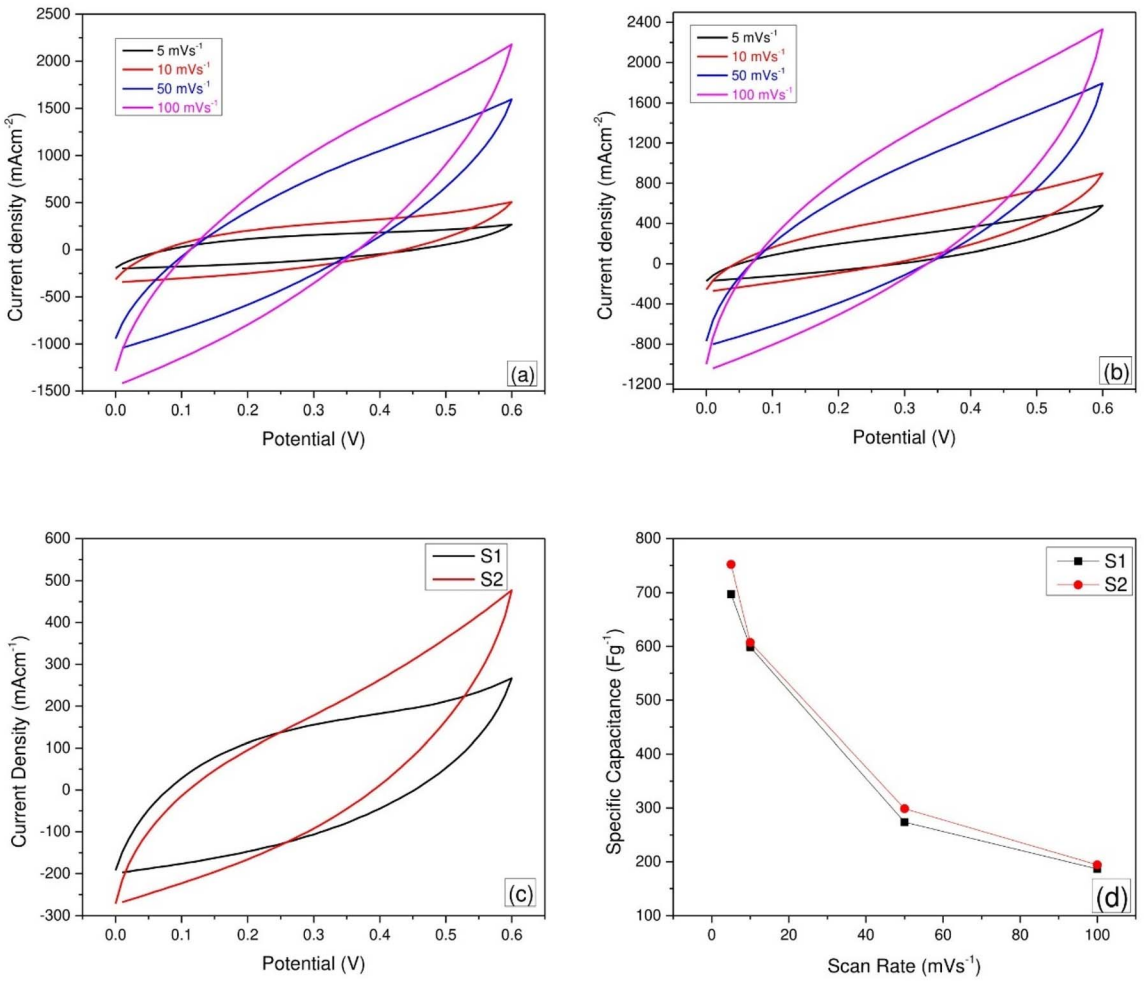

Fig. 8 (a) CV curves of S1, (b) CV curves of S2, (c) comparison of the CV curves of S1 and S2 at 5 mV s^{-1} and (d) comparison of the specific capacitance of S1 and S2 at different scan rates.

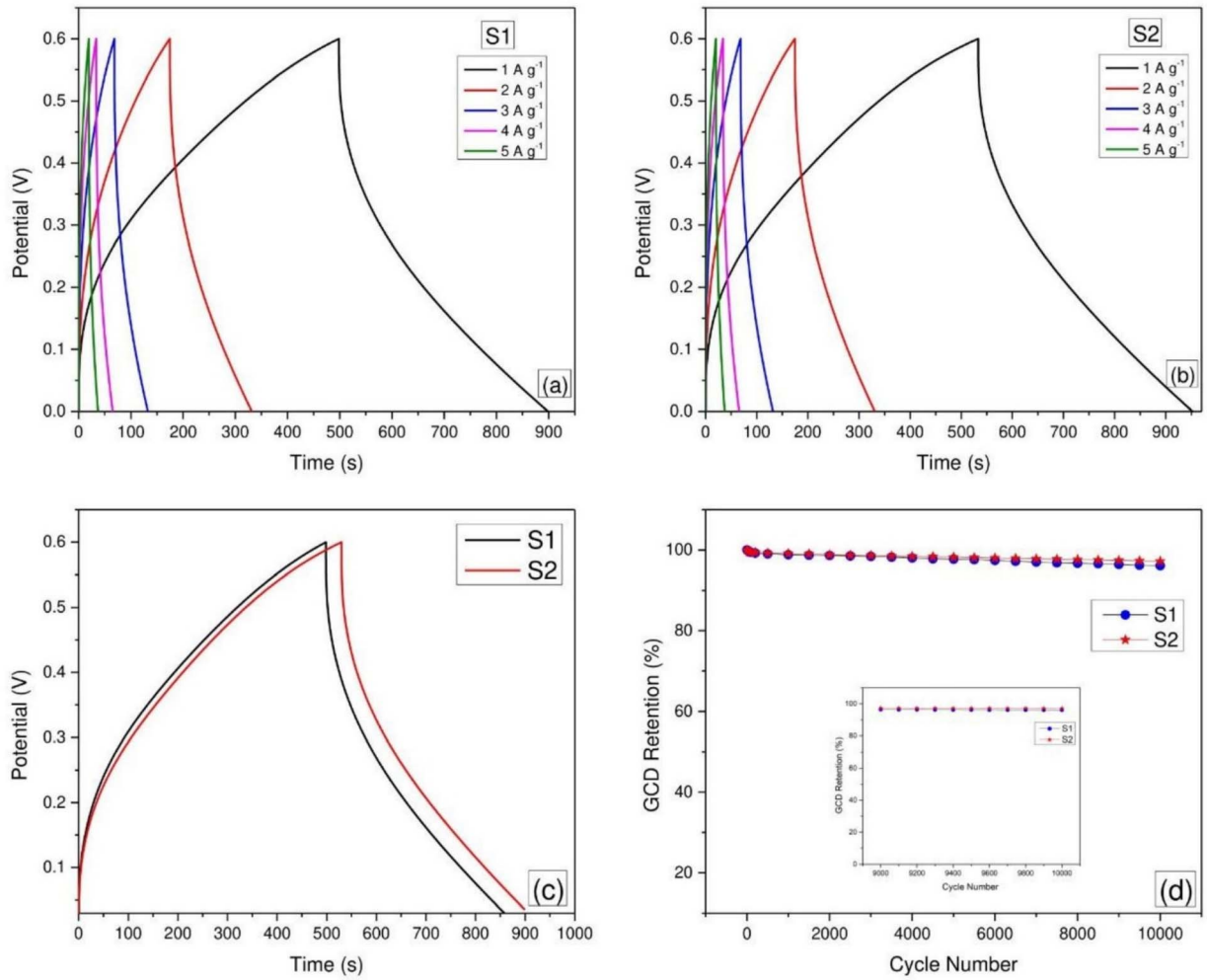

Fig. 9 (a) GCD curves of sample S1, (b) GCD curves of sample S2, (c) comparison of the GCD curves of S1 and S2 at 1 A g^{-1} and (d) cyclic stability curves of S1 and S2 at 5 A g^{-1}.

scan rate, indicating improved surface-controlled charge storage kinetics. This shift suggests that Mo doping effectively promotes faster charge transfer and increases the pseudocapacitive behavior, making S2 more favorable for high-rate SC applications.[70]

$$i = k_1 v + k_2 v^{1/2} \quad (6)$$

Here, i is the CV current at any given potential, $k_1 v$ represents the capacitive contribution and $k_2 v^{1/2}$ represents the diffusion-controlled contribution of charge.[71] In the CV plots, a discontinuity near zero potential is observed, which is likely due to the rapid switching of the scan direction. It may also arise due to instrumental artifacts like *iR* drop and capacitive offsets. It can be minimized by optimization of the potential window and scan rates.

4.5.2 Galvanostatic charge discharge (GCD) analysis. To further evaluate the electrochemical performance of the fabricated devices made from samples ZnV_2O_4 and $ZnV_{0.98}Mo_{0.02}O_2$, Galvanostatic Charge Discharge (GCD) analysis was done. Fig. 9 shows the GCD plots of the synthesized pure and Mo-doped samples S1 and S2 in 1 mol per L Na_2SO_4 electrolyte at a current density of 0.1 mA cm^{-2} and potential window ranging between 0 and 0.6 V. The asymmetrical galvanostatic charge–discharge (GCD) curves of the as-prepared electrode materials at different current densities are an indication of the pseudocapacitive behavior of the materials. This suggests that the charge storage process is governed by a fast and reversible surface or near-surface faradaic redox reactions.[72,73] The sample prepared by Mo-doping has a longer discharge time than sample S1 due to the significant electrolyte ion exchange between the electrode and electrolyte interface.[74] GCD calculations of the pure and doped samples at a current density of 1 mA cm^{-2} revealed that their maximum specific capacitances for S1 and S2 were 667 F g^{-1} and 700 F g^{-1}, respectively, which are inconsistent with the CV results. Pure sample S1 showed a higher value of energy density of 34.85 Wh kg^{-1} at a power density of 313.71 W kg^{-1}, while the Mo-doped sample S2 exhibited an energy density of 37.60 Wh kg^{-1} at a power density of 323.08 W kg^{-1}. Moreover, the as-fabricated device exhibits

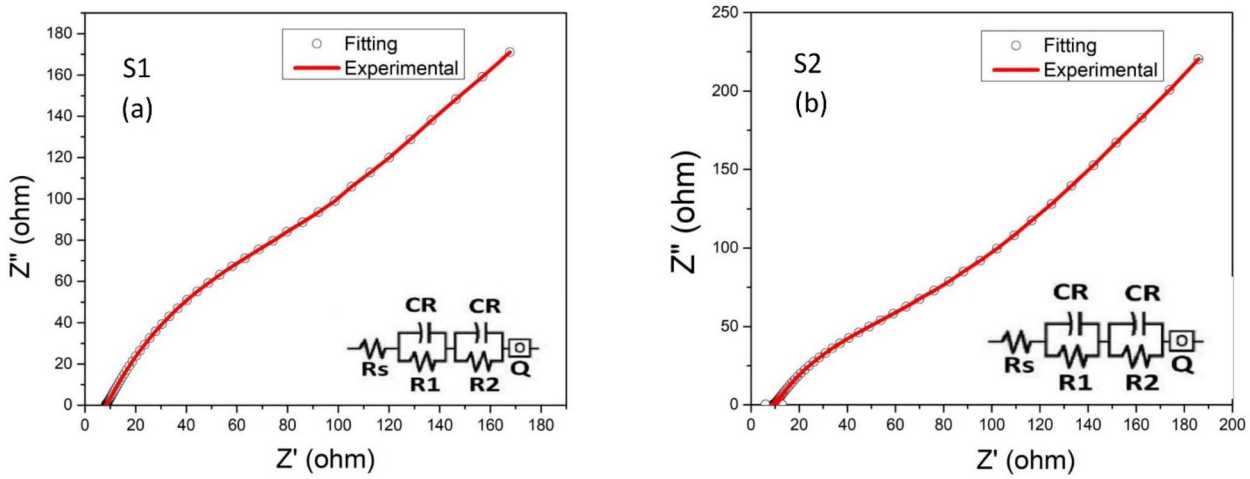

Fig. 10 EIS curves of samples (a) S1 and (b) S2.

excellent cyclic stability of 96.1% and 97.2% at 5 A g^{-1} after 10 000 cycles of charge and discharge for the pure and Mo-doped samples. This shows that Mo doping enhances the charge storing capability of ZnV_2O_4. This results in enhanced electronic conductivity and ion diffusion for better electrochemical performance. Fig. 9(c and d) shows the comparison of the GCD curves of S1 and S2 at 1 A g^{-1} and cyclic stability at 5 A g^{-1} after 10 000 cycles of charge–discharge, respectively.

4.5.3 Electrochemical impedance spectroscopy (EIS) analysis. Electrochemical impedance spectroscopy (EIS) in the frequency range of 1 mHz to 1 MHz using 1 mol per L Na_2SO_4 electrolyte was used to study the prepared devices, employing the synthesized samples S1 and S2. Fig. 10 displays the Nyquist plots and equivalent circuits of the devices made from samples S1 and S2. The excellent pseudocapacitive qualities of the pure and Mo-doped electrode materials can be seen by the straight line in the Nyquist spectra of the samples. Both spectra show a low charge transfer resistance of the materials. The electrolyte resistance and charge transfer resistance of Mo-doped sample S2 are considerably lower than that of sample S1, as seen by the Nyquist plot of the samples in low frequency areas. The charge transfer resistance (R_{ct}) drops from 59.3 Ω to 29.3 Ω for the Mo-doped sample. It shows improved electron mobility at the electrode–electrolyte interface and increased electrical conductivity. Additionally, for the Mo-doped material, the double-layer capacitance (C_{dl}) rose from 2.6 mF to 5.4 mF, suggesting enhanced interfacial charge accumulation. This is beneficial for the rapid cycles of charging and discharging. More importantly, with the Mo-doped sample, the Warburg impedance dropped to 0.58 Ω and the faradaic capacitance (C_F) rose to 543 mF. It indicates that the Mo-doped sample has better ion transport and higher redox activity. Table 3 summarizes the fitting parameters obtained from equivalent circuits.

The EIS results are consistent with the CV and GCD analysis results, indicating that the Mo-doped electrode material (S2) has low resistance and facilitates easier access for the intercalation and de-intercalation of charges between the electrode and electrolyte for better electrochemical performance.[75] Table 4 shows a comparison of the performance parameter of the proposed material with previously reported works.

Table 3 EIS fitting parameters of sample S1 and S2

Fitting parameters		R_s (Ω)	R_{ct} (Ω)	C_{dl} (mF)	W (Ω)	C_F (mF)
Samples	S1	10.01	59.3	2.6	0.85	268
	S2	9.03	29.3	5.4	0.58	543

Table 4 Performance comparison of the proposed material with the previously reported materials based on molybdenum

Electrode material	Specific capacitance	Cyclic stability	Energy density	Power density	Ref.
$PAC/MoO_2/Mo_2C$	74.7 F g^{-1}	83% after 25 000 cycles	51.8 Wh kg^{-1}	0.9 kW kg^{-1}	76
TiMoNi-oxides	255.4 F g^{-1}	96.8% after 11 000 cycles	68.47 Wh kg^{-1}	2058 W kg^{-1}	77
MnVMo-oxide	814.5 mF cm^{-2}	71.45% after 9000 cycles	0.025 mWh cm^{-2}	1.5 mW cm^{-2}	43
$NiMoO_4 \cdot xH_2O$	156 F g^{-1}	81% after 5000 cycles	55.6 Wh kg^{-1}	640 W kg^{-1}	41
Bi_2MoO_6@Ni foam	655.5 mF cm^{-2}	82% after 5000 cycles	22.76 × 10^{-3} Wh cm^{-2}	347.18 × 10^{-3} W cm^{-2}	78
$RGO(MP)_8$	363 F g^{-1}	73.4% after 200 cycles	72.6 Wh kg^{-1}	217.7 W kg^{-1}	79
ZnV_2O_4	697.14 F g^{-1}	96.1% after 10 000 cycles	34.85 Wh kg^{-1}	313.71 W kg^{-1}	This work
$ZnV_{0.98}Mo_{0.02}O_2$	752.08 F g^{-1}	97.2% after 10 000 cycles	37.60 Wh kg^{-1}	323.08 W kg^{-1}	This work

5. Conclusion

In conclusion, we have successfully synthesized pure and Mo-doped ZnV_2O_4 electrode materials using the hydrothermal method and fabricated a symmetric supercapacitor device. FESEM and EDX analysis of the prepared materials confirm spinel structures and purity of the synthesized materials. XRD and FTIR analysis confirm the high crystallinity and presence of functional groups, respectively, for better electrochemical performance. BET analysis shows good surface area values of 77.25 and 100.42 $m^2\ g^{-1}$ for the pure and Mo-doped samples, respectively. The as-prepared electrode materials provide promising pseudocapacitance performance by delivering a high energy density of 34.85 Wh kg^{-1} at a power density of 313.71 W kg^{-1} for S1 and 37.60 Wh kg^{-1} at a power density 323.08 W kg^{-1} for S2. Moreover, the prepared SC devices possess excellent specific capacitances of 697.14 F g^{-1} and 752.08 F g^{-1} and excellent cyclic stabilities of 96.1% and 97.2% at 5 A g^{-1} after 10 000 cycles of charge and discharge for pure and Mo-doped ZnV_2O_4, respectively. It can be concluded that the addition of Mo in ZnV_2O_4 enhances the surface area, specific capacitance, energy density, power density and cyclic stability for better performance as an electrode material. The finding of these synthesized materials reveals the potential possibilities of ternary metal oxides in energy storage applications. The enhanced electrochemical performance of Mo-doped MnV_2O_4 is attributed to the synergistic effects of Mo incorporation, which simultaneously improves the electrical conductivity, redox activity, and structural stability. Mo doping introduces additional redox-active sites and facilitates faster charge transfer, leading to improved capacitance and electrochemical performance.

Author contributions

Pankaj Kumar Sharma: writing – original draft, formal analysis, experimental, performed the literature search and data analysis, conceptualization, methodology. Anshuman Sahai: supervision and writing – review & editing. Deepti Maikhuri: supervision and writing – review & editing. Santosh J. Uke: validation, resources. Somya Asthana: formal analysis. Yogesh Kumar: supervision, writing – review & editing, validation, proposed the idea for the work.

Conflicts of interest

The authors declare that there are no conflicts of interest.

Data availability

Data will be made available from the corresponding author upon reasonable request.

References

1 J. Wang and W. Azam, Natural resource scarcity, fossil fuel energy consumption, and total greenhouse gas emissions in top emitting countries, *Geosci. Front.*, 2024, **15**(2), 101757, DOI: **10.1016/j.gsf.2023.101757**.
2 Y. Majeed, *et al.*, Renewable energy as an alternative source for energy management in agriculture, *Energy Rep.*, 2023, **10**, 344–359, DOI: **10.1016/j.egyr.2023.06.032**.
3 D. Zhao, X. Guo, Y. Gao and F. Gao, An Electrochemical Capacitor Electrode Based on Porous Carbon Spheres Hybrided with Polyaniline and Nanoscale Ruthenium Oxide, *ACS Appl. Mater. Interfaces*, 2012, **4**(10), 5583–5589, DOI: **10.1021/am301484s**.
4 T. Brousse, D. Bélanger and J. W. Long, To Be or Not To Be Pseudocapacitive?, *J. Electrochem. Soc.*, 2015, **162**(5), A5185, DOI: **10.1149/2.0201505jes**.
5 S. A. Pawar, D. S. Patil and J. C. Shin, Electrochemical battery-type supercapacitor based on chemosynthesized Cu_2S–Ag_2S composite electrode, *Electrochim. Acta*, 2018, **259**, 664–675, DOI: **10.1016/j.electacta.2017.11.006**.
6 T. Anitha, A. E. Reddy, R. Vinodh, H.-J. Kim and Y.-R. Cho, Preparation and characterization of $CoWO_4$/$CoMn_2O_4$ nanoflakes composites on Ni foam for electrochemical supercapacitor applications, *J. Energy Storage*, 2020, **30**, 101483, DOI: **10.1016/j.est.2020.101483**.
7 C. Wu, C. Chen, H. Zhang, Y. Tan and H. Yu, Preparation of magnesium oxysulfate cement using magnesium-rich byproducts from the production of lithium carbonate from salt lakes, *Constr. Build. Mater.*, 2018, **172**, 597–607, DOI: **10.1016/j.conbuildmat.2018.04.005**.
8 D. Chen, Q. Wang, R. Wang and G. Shen, Ternary oxide nanostructured materials for supercapacitors: a review, *J. Mater. Chem. A*, 2015, **3**(19), 10158–10173, DOI: **10.1039/C4TA06923D**.
9 Y. Kumar, *et al.*, Advancement and current scenario of engineering and design in transparent supercapacitors: electrodes and electrolyte, *J. Nanopart. Res.*, 2021, **23**(5), 119, DOI: **10.1007/s11051-021-05221-5**.
10 M. K. Aslam and M. Xu, A Mini-Review: MXene composites for sodium/potassium-ion batteries, *Nanoscale*, 2020, **12**(30), 15993–16007, DOI: **10.1039/D0NR04111D**.
11 S. M. Mousavi, *et al.*, Recent advances in energy storage with graphene oxide for supercapacitor technology, *Sustainable Energy Fuels*, 2023, **7**(21), 5176–5197, DOI: **10.1039/D3SE00867C**.
12 S. Ali, *et al.*, The emergence of density functional theory for supercapacitors: Recent progress and advances, *J. Energy Storage*, 2023, **73**, 109100, DOI: **10.1016/j.est.2023.109100**.
13 Bharti, *et al.*, Theories and models of supercapacitors with recent advancements: impact and interpretations, *Nano Express*, 2021, **2**(2), 022004, DOI: **10.1088/2632-959X/abf8c2**.
14 J. Huang, *et al.*, Rational Design of Electrode Materials for Advanced Supercapacitors: From Lab Research to Commercialization, *Adv. Funct. Mater.*, 2023, **33**(14), 2213095, DOI: **10.1002/adfm.202213095**.
15 E. M. Abebe and M. Ujjihara, Simultaneous Electrodeposition of Ternary Metal Oxide Nanocomposites for High-Efficiency Supercapacitor Applications, *ACS Omega*, 2022, DOI: **10.1021/acsomega.2c00826**.

16 M. Jiang, Z. Hou, L. Ren, Y. Zhang and J.-G. Wang, Prussian blue and its analogues for aqueous energy storage: From fundamentals to advanced devices, *Energy Storage Mater.*, 2022, **50**, 618–640, DOI: 10.1016/j.ensm.2022.06.006.

17 P. K. Sharma, A. Sahai, D. Maikhuri, S. J. Uke, S. Asthana and Y. Kumar, Hydrothermally synthesized Mo-doped MnV_2O_4 electrode materials for supercapacitor applications, *Ionics*, 2025, **31**, 8663–8677, DOI: 10.1007/s11581-025-06481-0.

18 J. Liu, S. Zhao and X. Wu, Flexible electrochemical capacitor based NiMoSSe electrode material with superior cycling and structural stability, *Chin. Chem. Lett.*, 2024, **35**(7), 109059, DOI: 10.1016/j.cclet.2023.109059.

19 A. Tundwal, *et al.*, Developments in conducting polymer-, metal oxide-, and carbon nanotube-based composite electrode materials for supercapacitors: a review, *RSC Adv.*, 2024, **14**(14), 9406–9439, DOI: 10.1039/D3RA08312H.

20 Y. Liu, *et al.*, Latest advances of metal-organic frameworks-based materials for supercapacitors, *Sustainable Mater. Technol.*, 2023, **36**, e00588, DOI: 10.1016/j.susmat.2023.e00588.

21 L.-D. Ye, *et al.*, Effect of Proton Conduction on the Charge Storage Mechanism of a MOF as a Supercapacitor Electrode, *J. Phys. Chem. C*, 2021, **125**(42), 22951–22959, DOI: 10.1021/acs.jpcc.1c03690.

22 Y. Shao, *et al.*, Design and Mechanisms of Asymmetric Supercapacitors, *Chem. Rev.*, 2018, **118**(18), 9233–9280, DOI: 10.1021/acs.chemrev.8b00252.

23 Q. Zhao, *et al.*, $KNbTeO_6$ transparent ceramics prepared by the combination of pressure-less sintering and pseudo hot isostatic pressing, *J. Eur. Ceram. Soc.*, 2023, **43**(9), 4226–4231, DOI: 10.1016/j.jeurceramsoc.2023.03.025.

24 M. Z. Ansari, S. A. Ansari and S.-H. Kim, Fundamentals and recent progress of Sn-based electrode materials for supercapacitors: A comprehensive review, *J. Energy Storage*, 2022, **53**, 105187, DOI: 10.1016/j.est.2022.105187.

25 Bharti, *et al.*, Theories and models of supercapacitors with recent advancements: impact and interpretations, *Nano Express*, 2021, **2**(2), 022004, DOI: 10.1088/2632-959X/abf8c2.

26 M. Czagany, *et al.*, Supercapacitors: An Efficient Way for Energy Storage Application, *Materials*, 2024, **17**(3), 702, DOI: 10.3390/ma17030702.

27 J.-S. Wei, T.-B. Song, P. Zhang, X.-Q. Niu, X.-B. Chen and H.-M. Xiong, A new generation of energy storage electrode materials constructed from carbon dots, *Mater. Chem. Front.*, 2020, **4**(3), 729–749, DOI: 10.1039/C9QM00554D.

28 P. K. Sharma, *et al.*, Recent Advancements in Ternary Metal Oxide-Based Electrode Materials for Supercapacitor Applications: A Review, *J. Electron. Mater.*, 2025, **54**(10), 8218–8238, DOI: 10.1007/s11664-025-12269-9.

29 J. Liu, *et al.*, MnO_2-based materials for supercapacitor electrodes: challenges, strategies and prospects, *RSC Adv.*, 2022, **12**(55), 35556–35578, DOI: 10.1039/D2RA06664E.

30 A. P. Khedulkar, V. D. Dang, A. Thamilselvan, R. Doong and B. Pandit, Sustainable high-energy supercapacitors: Metal oxide-agricultural waste biochar composites paving the way for a greener future, *J. Energy Storage*, 2024, **77**, 109723, DOI: 10.1016/j.est.2023.109723.

31 M. Z. Ansari, K.-M. Seo, S.-H. Kim and S. A. Ansari, Critical Aspects of Various Techniques for Synthesizing Metal Oxides and Fabricating Their Composite-Based Supercapacitor Electrodes: A Review, *Nanomaterials*, 2022, **12**(11), 1873–1900, DOI: 10.3390/nano12111873.

32 Y. Cao, *et al.*, Stability study of transition metal oxide electrode materials, *J. Power Sources*, 2023, **560**, 232710, DOI: 10.1016/j.jpowsour.2023.232710.

33 M. Cui, M. Pei and S. Kim, Recent advances in metal–organic framework-based inorganic composite electrodes for capacitors: a comprehensive review, *Adv. Ind. Eng. Chem.*, 2025, **1**(1), 8, DOI: 10.1007/s44405-025-00009-w.

34 I. Radja, *et al.*, Construction of a ternary composite of Mg-doped biochar/CuO, and PAni for supercapacitor applications, *J. Energy Storage*, 2025, **108**, 114785, DOI: 10.1016/j.est.2024.114785.

35 F. Mashkoor, M. Shoeb, S. Zhu, J. Ahmed, S. M. Noh and C. Jeong, Synergistic effect of heterointerface engineering coupled with oxygen vacancies enriched Ag_2O-$WO_{2.8}$-SnO_2 anchored carbon nanotubes nanocomposite for high-performance supercapacitor devices and their charge storage mechanism, *Surf. Interfaces*, 2025, **62**, 106198, DOI: 10.1016/j.surfin.2025.106198.

36 S. Kumari, *et al.*, A comprehensive review on various techniques used for synthesizing nanoparticles, *J. Mater. Res. Technol.*, 2023, **27**, 1739–1763, DOI: 10.1016/j.jmrt.2023.09.291.

37 Y.-Y. Huang and L.-Y. Lin, Synthesis of Ternary Metal Oxides for Battery-Supercapacitor Hybrid Devices: Influences of Metal Species on Redox Reaction and Electrical Conductivity, *ACS Appl. Energy Mater.*, 2018, **1**(6), 2979–2990, DOI: 10.1021/acsaem.8b00781.

38 C. S. Ferreira, R. R. Passos and L. A. Pocrifka, Synthesis and properties of ternary mixture of nickel/cobalt/tin oxides for supercapacitors, *J. Power Sources*, 2014, **271**, 104–107, DOI: 10.1016/j.jpowsour.2014.07.164.

39 B. Bhujun, M. T. T. Tan and A. S. Shanmugam, Study of mixed ternary transition metal ferrites as potential electrodes for supercapacitor applications, *Results Phys.*, 2017, **7**, 345–353, DOI: 10.1016/j.rinp.2016.04.010.

40 T. Xing, Y. Ouyang, Y. Chen, L. Zheng, C. Wu and X. Wang, P-doped ternary transition metal oxide as electrode material of asymmetric supercapacitor, *J. Energy Storage*, 2020, **28**, 101248, DOI: 10.1016/j.est.2020.101248.

41 G. Qu, *et al.*, Rapid and Scalable Synthesis of Mo-Based Binary and Ternary Oxides for Electrochemical Applications, *Adv. Funct. Mater.*, 2017, **27**(29), 1700928, DOI: 10.1002/adfm.201700928.

42 D. K. Denis, *et al.*, Solid Solution Engineering of Co–Ni-Based Ternary Molybdate Nanorods toward Hybrid Supercapacitors and Lithium-Ion Batteries as High-Performance Electrodes, *ACS Appl. Energy Mater.*, 2020, **3**(4), 3955–3965, DOI: 10.1021/acsaem.0c00353.

43 A. M. Teli, S. A. Beknalkar, S. M. Mane, M. A. Yewale, T. D. Dongale and J. C. Shin, Synergetic effect of ternary MnVMo-oxide electrode by hydrothermal method for high-

performance asymmetric supercapacitor, *J. Energy Storage*, 2023, **65**, 107289, DOI: 10.1016/j.est.2023.107289.

44 P. K. Sharma, A. Sahai, D. Maikhuri, S. J. Uke, S. Asthana and Y. Kumar, Exploring hydrothermal route for Mo-doped $ZnMn_2O_4$ ternary metal oxides electrode materials for supercapacitors, *J. Mater. Sci.: Mater. Electron.*, 2025, **36**(17), 1056, DOI: 10.1007/s10854-025-15157-4.

45 M. Z. U. Shah, *et al.*, Enhanced energy storage with TiO_2/NiO/ZnO core-shell heterostructures in hybrid battery-supercapacitor applications, *J. Alloys Compd.*, 2025, **1013**, 178548, DOI: 10.1016/j.jallcom.2025.178548.

46 J. Gupta, A. S. Ahmed, A. H. Anwer, A. Benamor, M. Z. Khan and A. Azam, GO optimization strategies for improved capacity retention in transition metal oxides based ternary nanocomposites for high-performance supercapacitors, *Mater. Today Commun.*, 2024, **39**, 108683, DOI: 10.1016/j.mtcomm.2024.108683.

47 A. A. Saleh, A. Amer, D. M. Sayed and N. K. Allam, A facile electrosynthesis approach of Mn-Ni-Co ternary phosphides as binder-free active electrode materials for high-performance electrochemical supercapacitors, *Electrochim. Acta*, 2021, **380**, 138197, DOI: 10.1016/j.electacta.2021.138197.

48 X. Zhang, A. Wu, X. Wang, C. Tian, R. An and H. Fu, Porous NiCoP nanosheets as efficient and stable positive electrodes for advanced asymmetric supercapacitors, *J. Mater. Chem. A*, 2018, **6**(37), 17905–17914, DOI: 10.1039/C8TA05551C.

49 N. Mansoor, *et al.*, A novel ternary Ag@MnCo-NGO-PVP hybrid composite for high performance asymmetric supercapacitors, *J. Energy Storage*, 2025, **112**, 115509, DOI: 10.1016/j.est.2025.115509.

50 M. Liu, H. Lin, L. Sun, Y. Ying, B. He and Y. Liu, Enhanced charge storage in supercapacitors using carbon nanotubes and *N*-doped graphene quantum dots-modified (NiMn)Co_2O_4, *J. Colloid Interface Sci.*, 2025, **678**, 763–771, DOI: 10.1016/j.jcis.2024.09.039.

51 J. Wang, *et al.*, Symmetric supercapacitors composed of ternary metal oxides ($NiO/V_2O_5/MnO_2$) nanoribbon electrodes with high energy storage performance, *Chem. Eng. J.*, 2021, **426**, 131804, DOI: 10.1016/j.cej.2021.131804.

52 C. Huang, *et al.*, Oxygen Vacancies Boosted Hydronium Intercalation: A Paradigm Shift in Aluminum-Based Batteries, *Angew. Chem., Int. Ed.*, 2024, **63**(26), e202405592, DOI: 10.1002/anie.202405592.

53 Z. Xiang, *et al.*, Improvement of magnetic properties and hardness by alloying Mo to a FeCrCo alloy, *Acta Mater.*, 2024, **281**, 120388, DOI: 10.1016/j.actamat.2024.120388.

54 A. Mendhe and H. S. Panda, A review on electrolytes for supercapacitor device, *Discover Mater.*, 2023, **3**(1), 29, DOI: 10.1007/s43939-023-00065-3.

55 A. Biswal, *et al.*, Role of Additives in Electrochemical Deposition of Ternary Metal Oxide Microspheres for Supercapacitor Applications, *ACS Omega*, 2020, **5**(7), 3405–3417, DOI: 10.1021/acsomega.9b03657.

56 M. Manikandan, E. Manikandan, V. Swetha, S. Kurpaa, S. Vijay and V. Kiruthika, Nickel-copper-cobalt mixed oxide electrode material for high performance asymmetric supercapacitor, *Sci. Rep.*, 2024, **14**(1), 10821, DOI: 10.1038/s41598-024-61625-y.

57 Y. Wang, D. Yang, J. Lian, T. Wei and Y. Sun, Ordered corn-like $CuCo_2O_4$ nanoforests covering Ni foam for a high-performance all-solid-state supercapacitor, *J. Alloys Compd.*, 2018, **741**, 527–531, DOI: 10.1016/j.jallcom.2018.01.168.

58 Y. Liu, *et al.*, Electroactivation-induced spinel ZnV_2O_4 as a high-performance cathode material for aqueous zinc-ion battery, *Nano Energy*, 2020, **67**, 104211, DOI: 10.1016/j.nanoen.2019.104211.

59 F. K. Butt, *et al.*, Synthesis of novel ZnV_2O_4 spinel oxide nanosheets and their hydrogen storage properties, *CrystEngComm*, 2013, **16**(5), 894–899, DOI: 10.1039/C3CE41859F.

60 T.-H. Wu, K.-Y. Ni, B.-T. Liu and S.-H. Wang, Activating ZnV_2O_4 by an Electrochemical Oxidation Strategy for Enhanced Energy Storage in Zinc-Ion Batteries, *ACS Appl. Energy Mater.*, 2022, **5**(8), 10196–10206, DOI: 10.1021/acsaem.2c01931.

61 P. Luo, *et al.*, Charged-optimized ZnO/ZnV_2O_4 composite hollow microspheres robust zinc-ion storage capacity, *J. Solid State Chem.*, 2021, **301**, 122371, DOI: 10.1016/j.jssc.2021.122371.

62 S. A. Hassanzadeh-Tabrizi, Precise calculation of crystallite size of nanomaterials: A review, *J. Alloys Compd.*, 2023, **968**, 171914, DOI: 10.1016/j.jallcom.2023.171914.

63 P. K. Sharma, A. Sahai, D. Maikhuri, S. J. Uke, S. Asthana and Y. Kumar, Effect on supercapacitive performance of Mo doped TEA assisted ternary metal oxides, *Interactions*, 2025, **246**(1), 71, DOI: 10.1007/s10751-025-02295-8.

64 A. Khalaf, R. Saghir, A. M. Abdallah, M. Noun and R. Awad, Influence of Mo doping on the structural, Raman scattering, and magnetic properties of NiO nanostructures, *Appl. Phys. A: Mater. Sci. Process.*, 2024, **130**(10), 691, DOI: 10.1007/s00339-024-07816-w.

65 Y. Qiu, *et al.*, Integration of pore structure modulation and B, N co-doping for enhanced capacitance deionization of biomass-derived carbon, *Green Energy Environ.*, 2023, **8**(5), 1488–1500, DOI: 10.1016/j.gee.2023.01.005.

66 S. Zafar and B. Lochab, Unleashing Vanadium-Based Compounds for High-Energy Aqueous Zinc–Ion Batteries, *ACS Omega*, 2024, **9**(49), 47920–47938, DOI: 10.1021/acsomega.4c06199.

67 Z. Gen, J. Yin, Y. Cheng and T. Yu, Nanostructure and Advanced Energy Storage: Elaborate Material Designs Lead to High-Rate Pseudocapacitive Ion Storage, *ACS Nano*, 2022, **16**(4), 5131–5152, DOI: 10.1021/acsnano.2c00557.

68 D. Shrestha, Evaluation of physical and electrochemical performances of hardwood and softwood derived activated carbons for supercapacitor application, *Mater. Sci. Energy Technol.*, 2022, **5**, 353–365, DOI: 10.1016/j.mset.2022.09.002.

69 V. Kushwaha, K. D. Mandal, A. Gupta and P. Singh, $Ni_{0.5}Co_{0.5}S$ nano-chains: a high-performing intercalating pseudocapacitive electrode in asymmetric supercapacitor (ASC) mode for the development of large-scale energy

storage devices, *Dalton Trans.*, 2024, **53**(12), 5435–5452, DOI: 10.1039/D3DT04184K.

70 C. Li, *et al.*, Morphology Modulation of $ZnMn_2O_4$ Nanoparticles Deposited In Situ on Carbon Cloth for Supercapacitors, *Metals*, 2024, **14**(8), 10682–10694, DOI: 10.3390/met14080841.

71 S. Li, *et al.*, Performance optimization of aqueous Zn/MnO_2 batteries through the synergistic effect of PVP intercalation and GO coating, *Chin. Chem. Lett.*, 2025, **36**(3), 110701, DOI: 10.1016/j.cclet.2024.110701.

72 M. C. Fite, P.-J. Wang and T. Imae, Symmetric and Asymmetric Supercapacitors of ITO Glass and Film Electrodes Consisting of Carbon Dot and Magnetite, *Batteries*, 2023, **9**(3), DOI: 10.3390/batteries9030162.

73 L. M. Da Silva, *et al.*, Reviewing the fundamentals of supercapacitors and the difficulties involving the analysis of the electrochemical findings obtained for porous electrode materials, *Energy Storage Mater.*, 2020, **27**, 555–590, DOI: 10.1016/j.ensm.2019.12.015.

74 D. Shao, *et al.*, Synthesis of porous Mn_2O_3 architecture for supercapacitor electrode application, *Colloids Surf., A*, 2023, **658**, 130532, DOI: 10.1016/j.colsurfa.2022.130532.

75 D. Li, Y. Dai, L. Kong, Y. Gu and L. Wang, Electrochemical induced Mo doping into graphene oxide supported vanadium-based materials for high performance aqueous zinc ion batteries, *J. Alloys Compd.*, 2023, **945**, 169324, DOI: 10.1016/j.jallcom.2023.169324.

76 N. F. Sylla, *et al.*, Enhanced Electrochemical Behavior of Peanut-Shell Activated Carbon/Molybdenum Oxide/Molybdenum Carbide Ternary Composites, *Nanomaterials*, 2021, **11**(4), DOI: 10.3390/nano11041056.

77 N. M. Deyab, M. M. Taha and N. K. Allam, A mesoporous ternary transition metal oxide nanoparticle composite for high-performance asymmetric supercapacitor devices with high specific energy, *Nanoscale Adv.*, 2022, **4**(5), 1387–1393, DOI: 10.1039/D1NA00694K.

78 U. T. Nakate, P. Patil, Y. T. Nakate, S.-I. Na, Y. T. Yu and Y.-B. Hahn, Ultrathin ternary metal oxide Bi_2MoO_6 nanosheets for high performance asymmetric supercapacitor and gas sensor applications, *Appl. Surf. Sci.*, 2021, **551**, 149422, DOI: 10.1016/j.apsusc.2021.149422.

79 X. Xia, Q. Hao, W. Lei, W. Wang, H. Wang and X. Wang, Reduced-graphene oxide/molybdenum oxide/polyaniline ternary composite for high energy density supercapacitors: Synthesis and properties, *J. Mater. Chem.*, 2012, **22**(17), 8314–8320, DOI: 10.1039/C2JM16216D.